

A Low Frequency Blind Survey of the Low Earth Orbit Environment using Non-Coherent Passive Radar with the Murchison Widefield Array

Prabu, S.^{1,3}, Hancock, P.¹, Zhang, X.² and Tingay, S.J.¹

¹International Centre for Radio Astronomy Research, Curtin University, Bentley, WA 6102, Australia

²CSIRO Astronomy and Space Science, 26 Dick Perry Avenue, Kensington, WA 6151, Australia

³CSIRO Astronomy and Space Science, Corner Vimiera & Pembroke Roads, Marsfield, NSW 2122, Australia

Abstract

We have extended our previous work to use the Murchison Widefield Array (MWA) as a non-coherent passive radar system in the FM frequency band, using terrestrial FM transmitters to illuminate objects in Low Earth Orbit (LEO) and the MWA as the sensitive receiving element for the radar return. We have implemented a blind detection algorithm that searches for these reflected signals in difference images constructed using standard interferometric imaging techniques. From 20 hours of archived MWA observations, we conduct a survey of LEO, detecting 74 unique objects over multiple passes and demonstrating the MWA to be a valuable addition to the global Space Domain Awareness network. We detected objects with ranges up to 977 km and as small as $0.03m^2$ radar cross section. We found that 30 objects were either non-operational satellites or upper-stage rocket body debris. Additionally, we also detected FM reflections from Geminid meteors and aircraft flying over the MWA. Most of the detections of objects in LEO were found to lie within the parameter space predicted by previous feasibility studies, verifying the performance of the MWA for this application.

Keywords: instrumentation: interferometers – planets and satellites: general – radio continuum: transients – techniques: radar astronomy

1 INTRODUCTION

With the advent of satellite mega-constellations, the density of objects in Low Earth Orbit (LEO) is predicted to reach 0.005 – 0.01 objects per degree square (McDowell, 2020). Most of the current space surveillance radar systems dedicated to monitoring such objects in space (Space Domain Awareness: SDA¹) operate at VHF/UHF/S-Band and utilise active transmitters to reflect signals from objects in the space environment (Goldstein et al., 1998). The predicted increase in the density of LEO objects demands detection systems with large instantaneous Field-of-View (FOV) receivers, the ability to change pointing directions and tracking quickly, and wide field illuminators. We aim to address these issues by using the Murchison Widefield Array (MWA) as a sensitive passive receiver in the FM band, coupled with existing, uncoordinated FM transmitters as the illuminators.

Previously, Prabu et al. (2020) developed a technique

using the so-called Dynamic Signal to Noise Ratio Spectrum (DSNRS) technique, that detects signals from satellites/debris, either via FM reflection or down-link transmission, and differentiates them from other types of Radio Frequency Interference (RFI) entering the detection system (the MWA). This previous work utilized the results of Zhang et al. (2018) to select a set of MWA observations known to contain signals reflected from satellites.

Having verified the DSNRS technique, we now take the next step in demonstrating SDA capabilities using the MWA, by developing and testing a semi-automated pipeline to perform uncued searches for the signals of interest. We test the pipeline on archival MWA data from observations in the FM band and we present here the results from the first low frequency non-coherent passive radar survey of LEO with the MWA. In this paper, we briefly summarise previous work in Section 2. We describe our data processing pipeline in Section 3, and our results in Section 4. The discussion and conclusions are in Sections 5 and 6, respectively.

¹Previously Space Situational Awareness (SSA)

2 BACKGROUND

Recently, many studies have raised concerns about the impacts of rapidly increasing LEO objects on astronomy (McDowell, 2020; Gallozzi et al., 2020; Hainaut & Williams, 2020; Mallama, 2020). We utilise this as an opportunity to demonstrate space surveillance capabilities using an existing radio interferometer and terrestrial FM transmitters.

The MWA is a low frequency radio interferometer built as a precursor to the Square Kilometre Array (SKA) (Tingay et al., 2013a). The MWA can observe the sky at 70 – 300 MHz and was primarily designed for radio astronomy purposes (Bowman et al., 2013; Beardsley et al., 2019). The MWA has detected satellites in the past using two different techniques; namely coherent detection (Palmer et al., 2017; Hennessy et al., 2019) and non-coherent detection (Tingay et al., 2013b; Zhang et al., 2018; Prabu et al., 2020) methods.

The coherent detection method uses the MWA’s high time and frequency resolution Voltage Capture System (VCS) (Tremblay et al., 2015) and performs detections using matched filters designed using the transmitted FM signal (Hennessy et al., 2019), while the non-coherent detection system uses interferometer correlated data (Prabu et al., 2020) along with wide-field imaging techniques. The blind detection pipeline developed here uses the non-coherent detection method, including the use of the DSNRS techniques established by Prabu et al. (2020).

Electromagnetic simulations presented in Tingay et al. (2013b) predict that LEO objects with a radar cross section (RCS) greater than $0.79 m^2$ and with line of sight (LOS) range less than 1000 km can be detected using the MWA in the FM band using non-coherent techniques, and we compare our obtained results with these predictions in Section 5.

3 DATA PROCESSING

In this work, we aimed to autonomously search for signals from satellites in the MWA data using non-coherent techniques. We utilised observations that observed the sky in the frequency range 72.335 – 103.015 MHz, as this band partially overlapped with FM frequencies and a large number of observations in this band were readily available in the MWA archive. The 628 observations (Table 1) used in this work were zenith pointing drift scans from four different nights performed using the MWA’s phase 2 compact configuration (Wayth et al., 2018). The compact configuration has most of its baselines shorter than 200 m, thus enabling the detection system to be sensitive towards near-field objects at FM frequencies.

The visibility files for these observations were downloaded from the All-Sky Virtual Observatory ² (ASVO)

²<https://asvo.mwatelescope.org/dashboard>

node for the MWA. They were converted to measurement sets (McMullin et al., 2007) using COTTER (Offringa et al., 2015) with a time averaging of 2 s and a frequency resolution of 40 kHz with RFI excision disabled.

Calibration observations were obtained as measurement sets from ASVO and were preprocessed with AOFLAGGER (Offringa et al., 2015) to flag all baselines with RFI. This was followed by calibration of the measurement sets using the calibrator model. Once calibrated, in order to obtain calibration solutions for channels with RFI, we interpolate solutions between neighbouring channels.

After applying the interpolated calibration solutions to the target observations, the measurement sets were imaged at every time-step and fine frequency channel using WSCLEAN (Offringa et al., 2014; Offringa & Smirnov, 2017). WSCLEAN is the abbreviation for W-Stack CLEANing, an advanced de-convolution method developed for wide-field interferometers. CLEAN (de-convolution) is usually done in order to reduce the side-lobes of the synthesised beam. However, we do not perform CLEAN as the subsequent step in our pipeline was to generate difference images, which remove the static celestial sources along with their side-lobes, revealing signals from objects such as satellites, meteors, and aircraft.

3.1 BLIND SEARCH

After the images at every time-step and frequency channels were generated, a blind detection pipeline was run. The pipeline constructed difference images by subtracting the image at time-step t from time-step $t + 1$, for every fine frequency channel, and searched for pixels over 6σ . The 6σ pixels were used to seed a detection, and we use a flood-fill³ function to identify all adjacent pixels above 3σ . An example of a satellite detected using this method is shown in Figure 1. The pixels together constitute the detected signal. We limit our algorithm to the detection of one event per time step per frequency, as when strong signals are present they are accompanied by many strong side-lobes, which we do not want to record as detections. Note that multiple detections at a single time-step are possible if they are seen in different frequency channels. Information for each detection, such as its coordinates (Right Ascension and Declination), peak flux density, time stamp, and frequency were stored for later analysis.

3.2 Detection Maps

For each of the target observations, the positions of the detections were combined to make detection maps as

³An algorithm that finds all adjacent cells that satisfy a given condition. We utilised the "forest fire algorithm" (Torbert, 2016).

Observation IDs	Start UTC	End UTC	Total Duration (hours)	Calibration Observation	Calibrator Source
1157366872 - 1157407072	2016-09-08 10:47:34	2016-09-08 21:57:34	1.93	1157381872	3C444
1157453032 - 1157493232	2016-09-09 10:43:34	2016-09-09 21:53:34	1.87	1157452432	Her A
1160477632 - 1160507152	2016-10-14 10:53:34	2016-10-14 19:05:34	7.34	1160507272	Pic A
1165749976 - 1165782976	2016-12-14 11:25:58	2016-12-14 20:35:58	8.4	1165779136	Hyd A

Table 1 List of observations and calibrator observations used in this work. Observation IDs can be searched within the MWA ASVO.

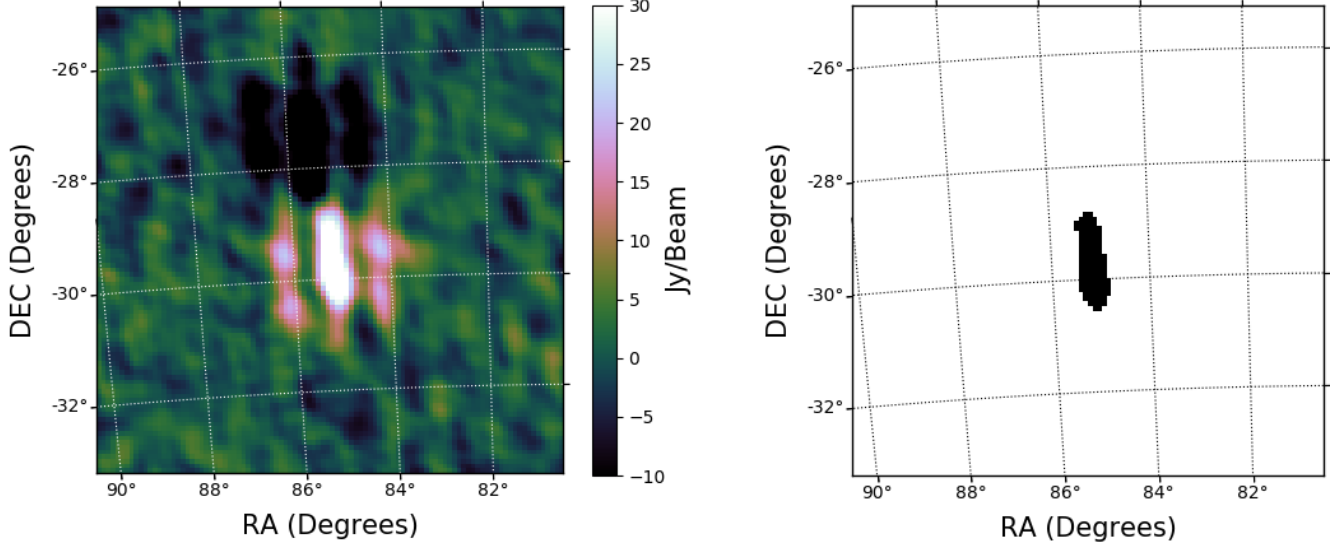


Figure 1. The left panel shows a primary beam corrected 40 kHz fine channel difference image of KANOPUS-V. KANOPUS-V is an Earth observation mini satellite orbiting at an altitude of 510 km. The image shows two adjacent streaks caused by side-lobes. The right panel shows the floodfill region of the detected signal.

shown in Figure 2. These detection maps are a visualisation tool to perform matching (by eye) of the detections in the observation with the predicted orbits of satellites in the FOV. In Figure 2 the detections are shown in black. The predicted trajectories⁴ for all the objects in LEO, Middle Earth Orbit (MEO), and Highly Elliptical Orbits (HEO) above the horizon are plotted in red and green. Tingay et al. (2013b) predicts that the objects with range less than 1000 km and an RCS greater than 0.785 m^2 can be detected by the MWA. Hence, if the object is within the MWA’s half power beam and satisfies the above mentioned conditions, then the red trajectory is replaced by green (as these are theoretically detectable orbits). The detections that were seen in multiple frequencies (in order to reduce the false positive events as described in Section 4.5) can be classified as satellites, meteor candidates, aircraft, terrestrial transmitters, unknown objects, and false detections, and are discussed in Section 4.

3.3 Parallax Analysis

The detections classified as aircraft (Section 4.3) appeared bright enough to be detected outside the MWA’s primary beam and we estimate the range to these aircraft by performing parallax measurements. The MWA has 128 tiles, and splitting the array into two sub-arrays enables us to perform parallax measurements to some of these bright nearby events that are within the atmosphere.

The MWA compact configuration baselines were sorted in longitude, using the geometric centres of the baselines. Using this sorted list of baselines, the 1000 east-most baselines were combined to make an eastern aperture (ensemble of points in the UV plane) and the 1000 west-most baselines were combined to make a western aperture. The measurement sets for the eastern and western apertures were created by using the split⁵ task in Common Astronomy Software Applications (CASA⁶) by providing the baseline configuration for both the

⁴Using TLE obtained from <https://www.space-track.org>

⁵<https://casa.nrao.edu/docs/TaskRef/split-task.html>

⁶<https://casa.nrao.edu/>

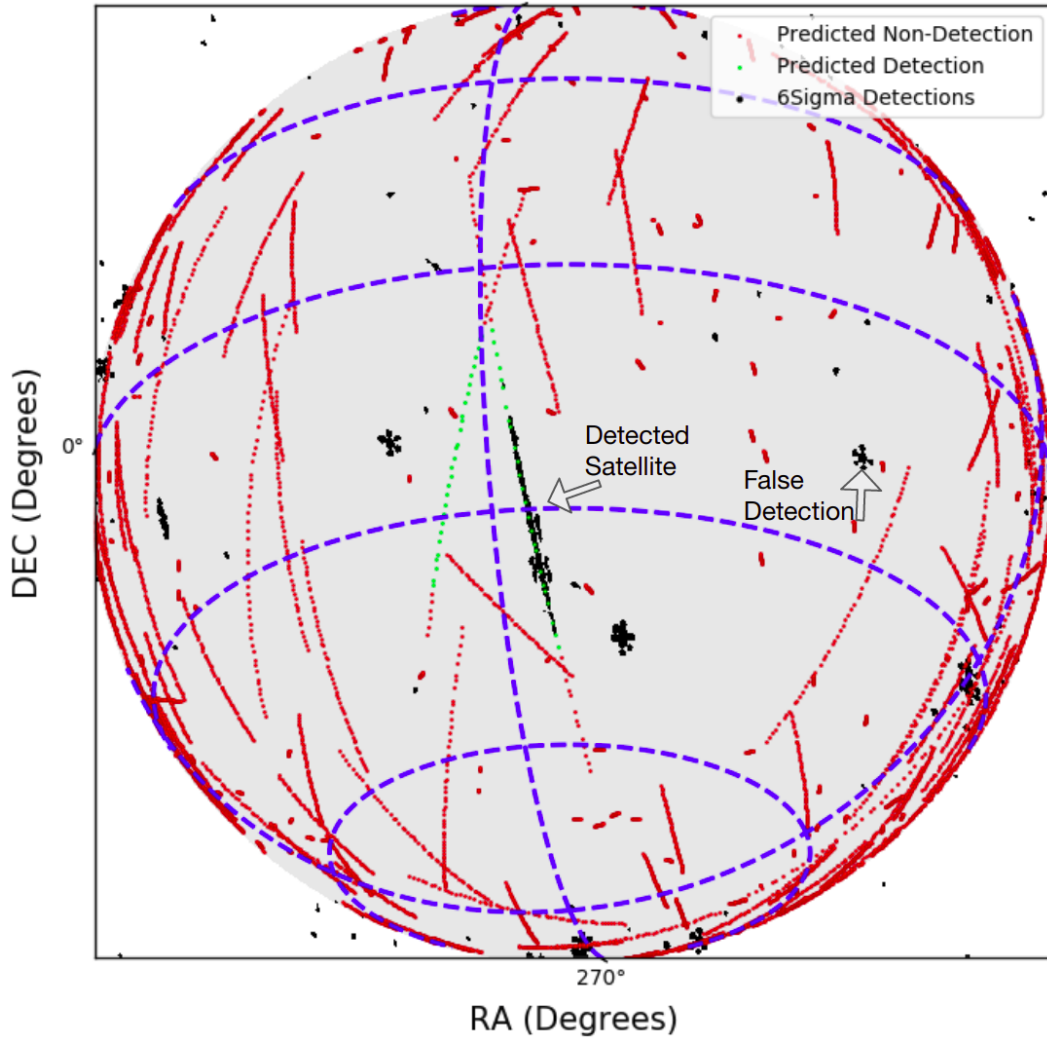


Figure 2. The image shows the visible horizon during one of the 112s MWA observations. The black markers are detections during this observation. The predicted orbits of all satellites within the visible horizon are plotted in red (or green). If the satellite orbit satisfies all predicted detection criteria (as predicted by Tingay et al. (2013b)) and is within MWA’s half power beam, then its trajectory is plotted in green. One of the theoretically detectable satellites being detected by the pipeline is shown and one is not detected. There are several transmitters also detected near the horizon. The figure also shows one of the false detections that takes the shape of the point spread function.

apertures.

Difference images for the full MWA compact array, eastern aperture, and western aperture were produced for one of the time-steps in which an aircraft was present. However, the UV coverages of the three apertures are different, resulting in different beams sizes. Hence, we address the problem by performing CLEAN and using a low resolution restoring beam corresponding to the lowest resolution of the three apertures. Due to the reflection signal being present in many frequency channels, we enabled the multi-frequency synthesis feature of WS-CLEAN while imaging. The centres of the eastern and western apertures were calculated using the geocentric coordinates of the tiles obtained from the measurement

set using casa-core⁷. The two apertures result in a parallax baseline of 228.2 m.

The difference images made using the eastern and western apertures showed the parallax shift in the apparent position of the aircraft, as shown in Figure 3. Using the maximum brightness points and the centres of the two apertures, the LOS range to the aircraft was calculated as in Earl (2015) to be 20 ± 2 km. The aircraft was detected at an azimuth of 82.6° and an elevation of 26.3° , placing it at an altitude of 9 ± 1 km (height of most civil aircraft). Note that although the baselines were sorted in longitude to maximise the East-West separation, the centres of the two apertures have a latitude

⁷<https://casacore.github.io/python-casacore/>

component as well, thus in Figure 3 we see a combination of East-West and North-South offsets in the apparent position.

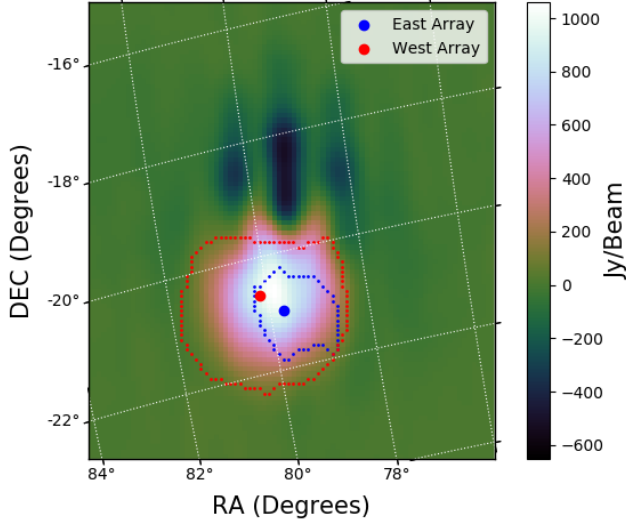


Figure 3. 30.72 MHz bandwidth difference image of an aircraft using the MWA compact array. The blue and the red dotted lines are 3σ contours of the streak when seen by the eastern and western apertures, respectively. The dots are the corresponding points of maximum brightness. Note that the contour of the eastern aperture image is smaller than that for the western aperture, due to the two sub-arrays having different sensitivities (number of short baselines) towards the aircraft’s altitude.

4 RESULTS

4.1 Satellite Candidates

Visual inspection of the detection maps for each of the observations was performed, and the events that plausibly matched in time and position with known objects at multiple time-steps were classified as satellite candidate detections. A total of 74 unique LEO objects were detected over multiple passes, of which 15 were upper stage rocket body debris. The LOS ranges for these satellites were obtained for the time-steps they were detected (calculated using the Two Line Element (TLE) values). The range values, along with RCS, peak flux densities, and operational statuses for these detected objects are tabulated in Table 2. An example DSNRS plot, illustrating the range of frequencies and times for which a satellite was detected is shown in Figure 4.

Two satellites, the CubeSats DUCHIFAT-1 and UKUBE-1, were detected due to out-of band transmissions in the FM band, rather than reflections (as previously observed by Zhang et al. (2018) and Prabu et al. (2020)).

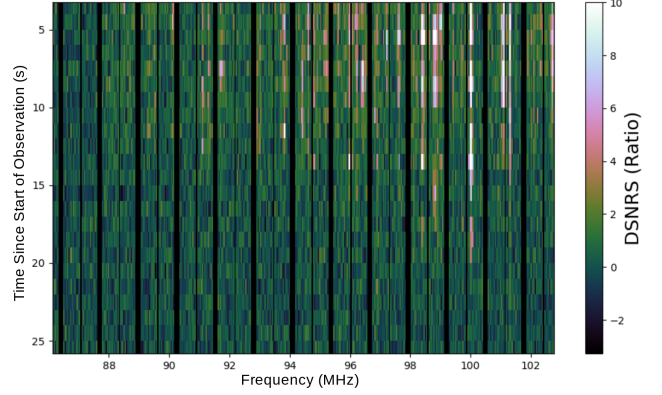


Figure 4. DSNRS plot for ZIYUAN 3 (ZY 3). The plot shows the different FM frequencies reflected by the satellite. The black vertical lines in the figure are due to the flagging of trailing, central, and leading fine frequency channels in every coarse channel.

4.2 Meteor Candidates

The observations from one of the nights used in this work (14th December 2016) coincided with the Geminids meteor shower. The pipeline detected many reflections from objects that had angular speeds much greater than expected for LEO objects. These objects moved approximately 10 degrees in a single 2 s time-step and are FM reflections from the ionised trails of meteors, as previously observed by Zhang et al. (2018) with the MWA. An example is shown in Figure 5. These events often appeared much brighter than satellites and were often pointing in the direction of the Geminids radiant.

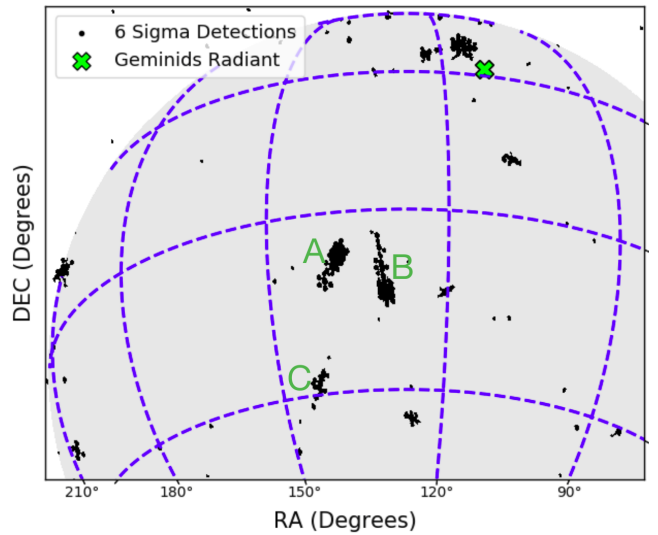


Figure 5. Three of the detected meteors are shown in regions A, B and C. Meteor-A and meteor-C point in the direction of the Geminids Radiant while meteor-B could be a sporadic meteor.

Table 2 Detected Satellites/Debris and their properties.

Observation ID	NORAD ID	Satellite/Debris Name	Range km	RCS m^2	Operational Status	θ Degrees	Peak Flux Density (Jy/beam)
The detections below are from the night of 2016-12-14 from 11:25:58 UTC to 20:35:58 UTC							
1165782616	33408	SJ-6E	598 - 603	1.3	O	5.0	32.5
1165782016	28898	MOZHAYETS 5 and RUBIN-5	699 - 709	5.9	N/A	2.3	31.2
1165780696	23088	SL-16 R/B	863 - 873	10.3	R/B	13.4	137.9
1165779376	13367	LANDSAT 4	538 - 539	6.4	NO	6.3	35.3
1165777336	28230	GP-B	669 - 687	10.2	NO	9.9	61.3
1165777216	9786	DELTA 1 R/B(1)	621 - 624	8.9	R/B	6.5	55.4
1165776496	40420	COSMOS 2503	587 - 600	5.5	O	3.1	33.6
1165773496	40310	YAOGAN 24	639 - 656	4.2	O	3.3	115.8
1165773136	24277	MIDORI (ADEOS)	806 - 816	22.2	NO	5.8	51.2
1165772296	13153	COSMOS 1356	480 - 486	9.0	N/A	7.3	39.9
1165771216	33492	GOSAT (IBUKI)	681 - 705	4.6	O	5.1	56.3
1165771096	33053	FGRST (GLAST)	555 - 563	4.9	E	17.7	233.9
1165770136	41336	BREEZE-KM R/B	534 - 540	3.3	R/B	20.0	38.2
1165768696	20580	HST	617 - 669	28.1	O	25.2	449.5
1165767856	25078	IRIDIUM 44	780 - 783	3.3	NO	6.2	44.5
1165766176	38707	KANOPUS-V 1	518 - 543	1.9	O	5.7	81.9
1165765696	41731	QSS (MOZI)	528 - 540	2.1	O	20.8	50.5
1165765336	39152	TURKSAT-3USAT	632 - 642	0.1	NO	3.9	25.5
1165765216	25544	ISS (ZARYA)	651 - 877	399.1	O	47.2	247,009
1165765096	25544	ISS (ZARYA)	733 - 977	399.1	O	44.4	25,936
1165764136	25758	IRS-P4 (OCEANSAT)	730 - 764	3.5	NO	0.9	44.8
1165764136	28499	ARIANE 5 R/B	687 - 698	16.0	R/B	13.0	45.1
1165763056	39019	PLEIADES 1B	719 - 729	5.4	O	8.2	26.7
1165762576	20580	HST	578 - 600	28.1	O	19.9	120.6
1165761856	41848	WORLDVIEW-4	626 - 634	6.6	PO	5.3	30.2
1165761736	27601	H-2A R/B	844 - 879	24.6	R/B	5.9	34.8
1165761376	41341	H-2A R/B	576 - 607	27.4	R/B	8.5	127.1
1165761256	38046	ZIYUAN 3 (ZY 3)	528 - 561	5.3	O	13.7	139.3
1165761136	38046	ZIYUAN 3 (ZY 3)	513 - 562	5.3	O	5.8	152.1
1165760896	21422	COSMOS 2151	618 - 625	5.7	N/A	9.2	26.5
1165760776	12987	COSMOS 1328	565 - 579	8.2	N/A	6.5	44.2
1165760536	38249	PSLV R/B	381 - 407	5.8	R/B	1.4	55.0
1165758616	29499	METOP-A	862 - 878	11.2	O	17.1	53.0
1165757056	27386	ENVISAT	782 - 805	18.6	NO	8.0	117.6
1165756576	20580	HST	565 - 584	28.1	O	13.4	59.0
1165756576	29228	RESURS-DK 1	583 - 596	8.8	O	13.0	25.7
1165756456	20580	HST	551 - 553	28.1	O	8.3	80.8
1165756096	11060	TIROS N	849 - 853	4.1	PO	0.8	37.2
1165755976	14819	COSMOS 1544	505 - 526	8.3	N/A	0.3	179.8
1165754896	32062	CBERS 2B	773 - 784	2.5	NO	12.7	38.4
1165753936	16881	COSMOS 1766	558 - 584	8.3	N/A	3.3	52.3
1165753936	23968	ATLAS 2 CENTAUR R/B	472 - 528	14.9	R/B	5.2	242.6
1165752856	16613	SPOT 1	691 - 702	7.3	NO	15.4	102.4
The detections below are from the night of 2016-10-14 from 10:53:34 UTC to 19:05:34 UTC							
1160505472	38257	YAOGAN 14	493 - 505	5.41	O	7.5	143.0
1160504512	10490	DELTA 1 R/B(1)	523 - 530	9.1	R/B	9.3	48.1

Continued on next page...

Table 2 ...continued from previous page.

Observation ID	NORAD ID	Satellite/Debris Name	Range km	RCS m ²	Operational Status	θ Degrees	Peak Flux Density (Jy/beam)
1160504752	24796	IRIDIUM 4	805 - 815	3.7	NO	13.5	63.1
1160502952	21574	ERS-1	790 - 794	10.3	NO	4.4	32.7
1160502472	15427	NOAA 9	876 - 904	4.3	PO	13.4	61.8
1160500432	28480	CZ-2C	841 - 843	10.0	R/B	13.4	38.2
1160498872	36095	COSMOS 2455	914 - 917	12.2	O	2.9	41.8
1160497792	24950	IRIDIUM 31	793 - 800	3.6	N/A	2.3	35.1
1160497672	25544	ISS (ZARYA)	454 - 577	399.1	O	21.5	23,492
1160497672	40074	UKUBE-1	739 - 760	0.1	O	31.3	417.1
1160497552	25544	ISS (ZARYA)	442 - 587	399.1	O	17.9	19,138
1160497192	19274	OKEAN-1	573 - 586	8.6	N/A	7.7	49.6
1160497072	19274	OKEAN-1	564 - 575	8.6	N/A	4.0	40.2
1160497072	41386	RESURS P3	520 - 546	7.7	O	18.5	160.2
1160496352	39574	GPM-CORE	415 - 435	8.1	O	11.1	70.2
1160496232	39574	GPM-CORE	410 - 479	8.1	O	7.0	598.1
1160495752	23608	ARIANE 40+3 R	602 - 619	9.7	R/B	6.8	142.6
1160493592	40118	GAOFEN 2	642 - 714	3.5	O	3.4	126.3
1160493472	40021	DUCHIFAT-1	647 - 709	0.03	O	17.6	469.0
1160493472	25260	SPOT 4	716 - 752	6.2	NO	0.5	109.4
1160492512	28649	IRS-P5 (CARTOSAT-1)	654 - 668	4.7	O	15.4	105.6
1160492392	28649	IRS-P5 (CARTOSAT-1)	640 - 647	4.7	O	10.2	44.9
1160491192	20624	COSMOS 2082	864 - 888	10.8	N/A	11.1	146.4
1160490232	23697	ATLAS 2 CENTAUR	919 - 929	13.9	R/B	2.5	76.0
1160489512	812	OPS 4467 A	821 - 844	0.34	N/A	0.9	48.9
1160488792	27421	SPOT 5	659 - 665	7.3	NO	9.4	130.6
1160487952	41765	TIANGONG-2	446 - 455	15.8	N/A	28.4	232.9
1160487832	23317	OKEAN-4	639 - 656	7.1	N/A	9.5	208.3
1160486632	8845	METEOR 1-25	884 - 896	4.0	N/A	8.6	122.7
1160485792	39358	SHIJIAN-16 (SJ-16)	643 - 646	8.3	O	12.9	147.9
1160484112	28118	ATLAS 3B CENTAUR	313 - 349	11.9	R/B	10.3	174.6
1160479192	40913	CZ-6 R/B	460 - 465	2.6	R/B	7.5	61.4
The detections below are from the night of 2016-09-09 from 10:43:34 UTC to 21:53:34 UTC							
1157493232	41727	GAOFEN 3	790 - 811	3.9	O	14.7	256.4
1157486032	19549	IUS R/B(1)	298 - 303	11.8	R/B	14.9	1606
1157474632	20580	HST	551 - 583	28.1	O	9.3	1336.2
1157472832	35931	OCEANSAT-2	731 - 741	4.1	O	2.9	113.7
1157472832	41386	RESURS P3	479 - 489	7.7	O	1.6	121.9
1157468632	20580	HST	590 - 633	28.1	O	22.0	1306
The detections below are from the night of 2016-09-08 from 10:47:34 UTC to 21:57:34 UTC							
1157407072	41456	SENTINEL-1B	738 - 754	5.6	O	15.7	77.7
1157407072	32382	RADARSAT-2	804 - 812	8.4	O	4.4	45.0
1157394472	41026	YAOGAN 28	505 - 563	4.8	O	16.5	672.3
1157393872	20978	DMSP 5D-2 F10 (USA 68)	840 - 846	3.9	NO	16.4	47.4
1157383672	33504	KORONAS-FOTON	545 - 547	4.2	NO	2.6	47.2
1157382472	15944	COSMOS 1674	546 - 570	8.7	N/A	10.2	44.3

Legend: O=Operational, R/B=Rocket Body, NO=Non-Operational, PO=Partially Operational, N/A=Not Available. The table summarises the properties of all the detected satellites. It provides the satellite's North American Aerospace Defence (NORAD) ID, the range of distance over which it was detected, its Radar Cross Section (RCS⁸), the zenith angle (θ), and the primary beam corrected peak flux density as seen in the brightest 40 kHz frequency channel. Note that the operational status ⁹ may not be accurate as the information source does not list the date it was last updated. Note that the Observation ID is the GPS time of the start of the observation.

4.3 Aircraft

Nineteen aircraft passes were detected by the pipeline, due to their large reflecting areas and smaller ranges. Most of these aircraft flew North-South over the MWA (a very common flight path for flights between Singapore/Malaysia/northern WA locations and Perth). These reflections appeared very bright (approximately 2800 Jy/beam peak flux density in a 30.72 MHz bandwidth difference image) and we utilised parallax to determine their altitudes (Section 3.3).

4.4 Transmitters and Unknown Objects

Transmitters near the horizon were often detected. These transmitters are not removed through difference images as they are at a fixed azimuth and elevation, hence appear to move in celestial coordinates with time. In future observations, these azimuths/elevations will be masked in order to prevent the pipeline from detecting these transmitters. The transmitters are seen at multiple FM frequencies.

We also detected several events that had angular speeds very similar to LEO objects but did not coincide with any known orbits in the TLE catalog. These are likely to be either satellites with outdated TLEs or uncatalogued objects (intentionally or otherwise). In future, we will investigate these events further by performing orbit determination estimates.

4.5 False Positives

The noise in difference images mainly consists of thermal noise and is assumed to follow Gaussian statistics. Due to the large volume of data used in this work, thermal noise fluctuations can trigger the 6σ threshold of the detection pipeline, and hence it is important that we quantify these false positives. However, since we constrain the pipeline to allow only the brightest detection per time-step and per frequency channel, the number of false detections is reduced in the presence of a bright reflection event that is seen in multiple frequencies.

In order to investigate the number of false positives, we ran our pipeline again but only on the 380 fine channels outside the FM band (i.e outside 87.5 – 108 MHz, which is the FM band in Australia). By doing so, we only detect the false positives as the reflection events are confined to the FM band. Note that observations that had no transmitting satellites were used for this analysis, as the transmitted signals from satellites were not confined to the FM band.

We obtained an average of 13 false detections per minute, for the 380 fine frequency channels used. Thus for a full bandwidth observation, and in the absence of any satellite detection, we would obtain approximately 26 false detections per minute. However, since we utilise

other tools such as DSNRS (frequency and time analysis) and detection maps (position and time analysis), to investigate these events further, the probability of classifying one of these events as a LEO object is insignificantly small.

5 DISCUSSION

5.1 Detection Completeness

Tingay et al. (2013b) predicts that satellites with an RCS greater than $0.79 m^2$ and with LOS range less than 1000 km can be detected using the MWA in the FM band using non-coherent techniques. All the satellites/debris that passed through the MWA’s half power beam with a shortest range during a pass less than 2000 km were identified and their RCS, along with the shortest range during pass, are plotted in Figure 6. All of the detected objects in this work (except three CubeSats and one MiniSat) were detected within the theoretically predicted parameter space. Two of the CubeSats (DUCIFAT-1 and UKUBE-1) were detected due to out-of band transmissions in the FM band (as previously observed by Zhang et al. (2018) and Prabu et al. (2020)) and the other CubeSat and MiniSat were detected through FM reflections. Some satellites such as the ISS and Hubble Space Telescope (HST) were also detected outside the MWA’s primary beam due to their large RCS.

From Figure 6 it can be seen that not all the satellites in the predicted parameter space were detected. This could be due to a number of reasons, for example unfavourable reflection geometries, or our pipeline being constrained to allow only one detection per time step per frequency channel. One significant reason could be that the RCS values are estimated by the US Space Surveillance Network (SSN) (R. Sridharan, 1998) using VHF/UHF/S-Band radars and are very likely to be quite different at the FM frequencies considered in this work. The RCS can also vary drastically as the transmitter-target-MWA reflection geometry changes and as the satellite tumbles. Also, the radar measured RCS is usually for a direct back-scatter/reflection where the transmitter and the receiver are co-located, as opposed to our method where we are looking at an oblique scattering of radiation (bi-static radar). Hence, we use the cataloged RCS values as an order of magnitude guide only. Also, since the classification of an event as a LEO object is done by visual inspection, it is possible that we missed detections near the horizon as it is usually crowded with many orbits due to projection effects as seen in Figure 2.

From Table 2 we can see that many satellites, such as the HST, were detected multiple times on the same night, demonstrating the MWA’s re-acquisition capability for large objects. Many objects such as rocket body debris and non-operational satellites were also detected,

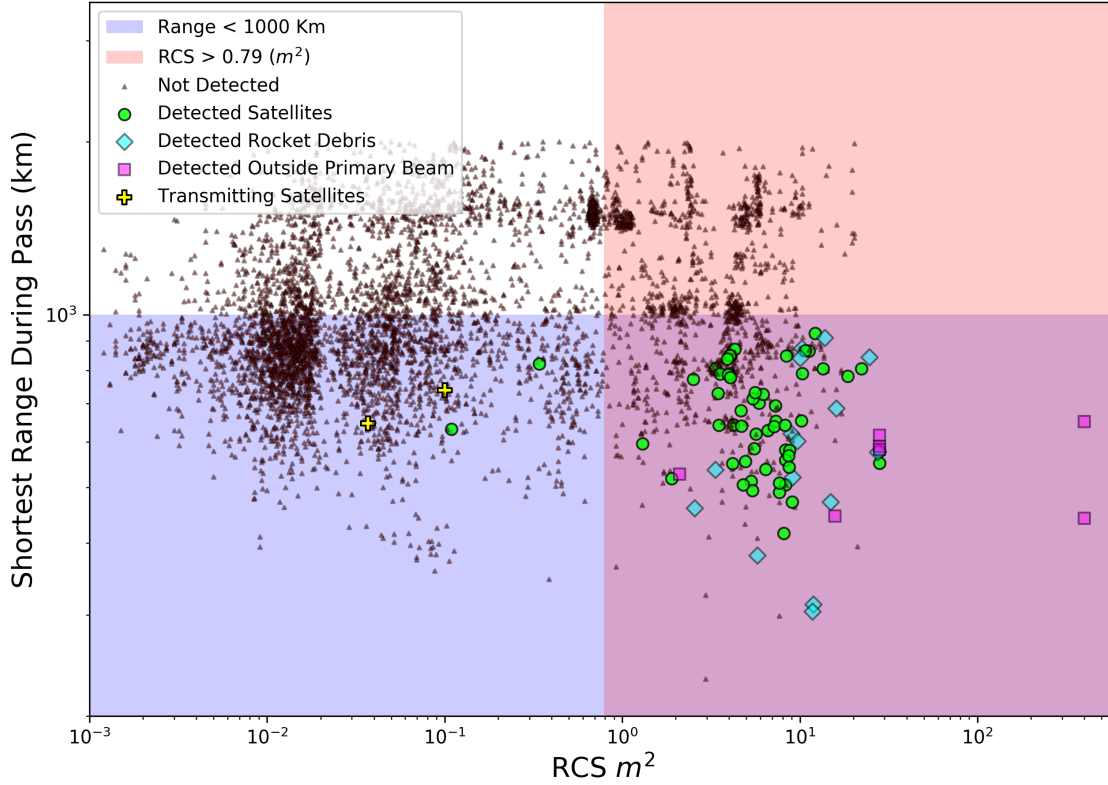


Figure 6. The RCS and the shortest range for all the satellites/debris passes above the horizon within the half power beam and with a range less than 2000 km. Note that although a satellite can appear in two consecutive observation IDs, it appears in the above plot as a single datum e.g. the ISS is detected in four observations according to Table 2, but only appears twice in the above plot (two rightmost points with the largest RCS) because those four observations covered two passes.

and for these objects passive space surveillance is the only way we can track them, thus demonstrating the MWA’s utility to track large obsolete objects. One such example is the object OPS 4467 A (NORAD ID 812). This satellite is the oldest object detected in our work and was launched in 1964.

Other interesting detected objects from Table 2 are MOZHAYETS-5 and RUBIN-5, which were launched together on the same rocket. RUBIN-5 was designed to stay attached to the payload adapter while MOZHAYETS-5 failed to detach from the adapter and hence they appear together as a single object in Table 2.

In one of the observations, the ISS was detected near the horizon with a peak flux density of 247,009 Jy/beam in one of the 40 kHz fine frequency channels. This could be due to a favourable reflection geometry and reflections from its very large solar panel arrays.

6 CONCLUSIONS

We have built upon previous work using the MWA as a passive radar system by developing a semi-automated pipeline that searches for reflected signals from LEO satellites in high time and frequency resolution data. Previous detections were performed by manual inspection of full band-width difference images, and here we have dramatically increased the number of detections by searching autonomously in every fine frequency channel.

Testing our pipeline on archived MWA data, we detected more than 70 unique LEO objects in 20 hours of observation. DUCHIFAT-1 and UKube-1 were detected due to spurious transmissions, while every other detected object was due to FM reflections. The large number of satellite detections through FM reflections alone prove MWA to be a valuable future asset for the global SDA network.

All, except four, of the detected objects were found to lie within the parameter space (range vs RCS) predicted by [Tingay et al. \(2013b\)](#). However, not all objects that

were predicted to be detectable were detected. This could be due to a number of reasons such as tumbling and unfavourable reflection geometries reducing the RCS of the object.

Along with the many satellite detections, we also detected FM reflections from Geminid meteors and aircraft flying over the MWA. Some detected events had angular speeds similar to LEO objects but did not have a satellite orbit match. In the future, we will further examine these unidentified objects by performing orbit determination. We will also use our data to demonstrate a detailed LEO catalog maintenance capability. The Gauss orbit determination technique (Curtis, 2013) will be utilised, as we only measure the angular migration of the objects with non-coherent techniques. In future, the detection pipeline used here will be upgraded to perform fully autonomous detections instead of the visual inspection performed here.

Many satellites transmit at MWA frequencies for down-link telemetry. Hence, observing in these frequencies could expand our detection window beyond the feasible parameter space (RCS-range) shown in this work. The future detection and characterisation of satellites that unintentionally transmit out of band will also assist in determining the threat of mega-constellations of small satellites to ground-based radio astronomy facilities.

7 ACKNOWLEDGEMENTS

This scientific work makes use of the Murchison Radio-astronomy Observatory, operated by CSIRO. We acknowledge the Wajarri Yamatji people as the traditional owners of the Observatory site. Support for the operation of the MWA is provided by the Australian Government (NCRIS), under a contract to Curtin University administered by Astronomy Australia Limited. We acknowledge the Pawsey Supercomputing Centre which is supported by the Western Australian and Australian Governments. Steve Prabu would like to thank Innovation Central Perth, a collaboration of Cisco, Curtin University, Woodside and CSIRO's Data61, for their scholarship.

Software

We acknowledge the work and the support of the developers of the following Python packages: Astropy (The Astropy Collaboration et al., 2013; Astropy Collaboration et al., 2018), Numpy (van der Walt et al., 2011), Scipy (Jones et al., 2001), matplotlib (Hunter, 2007) and Ephem¹⁰. The work also used WSCLEAN (Offringa et al., 2014; Offringa & Smirnov, 2017) for making fits images and DS9¹¹ for visualization purposes.

REFERENCES

Astropy Collaboration et al., 2018, *The Astronomical*

Journal, 156, 123

Beardsley A. P., et al., 2019, arXiv e-prints, [p. arXiv:1910.02895](https://arxiv.org/abs/1910.02895)

Bowman J. D., et al., 2013, *PASA*, 30, e031

Curtis H. D., 2013, *Orbital mechanics for engineering students*. Butterworth-Heinemann

Earl M. A., 2015, *Determining the Range of an Artificial Satellite Using its Observed Trigonometric Parallax* ([arXiv:1504.00965](https://arxiv.org/abs/1504.00965))

Gallozzi S., Scardia M., Maris M., 2020, *Concerns about ground based astronomical observations: a step to safeguard the astronomical sky* ([arXiv:2001.10952](https://arxiv.org/abs/2001.10952))

Goldstein R., Goldstein S., Kessler D., 1998, *Planetary and Space Science*, 46, 1007

Hainaut O. R., Williams A. P., 2020, *Astronomy & Astrophysics*, 636, A121

Hennessy B., et al., 2019, in *2019 IEEE Radar Conference (RadarConf)*. pp 1–6, [doi:10.1109/RADAR.2019.8835821](https://doi.org/10.1109/RADAR.2019.8835821)

Hunter J. D., 2007, *Computing in Science & Engineering*, 9, 90

Jones E., Oliphant T., Peterson P., Others 2001, *SciPy: Open Source Scientific Tools for Python*

Mallama A., 2020, arXiv preprint [arXiv:2003.07805](https://arxiv.org/abs/2003.07805)

McDowell J. C., 2020, *The Low Earth Orbit Satellite Population and Impacts of the SpaceX Starlink Constellation* ([arXiv:2003.07446](https://arxiv.org/abs/2003.07446))

McMullin J. P., Waters B., Schiebel D., Young W., Golap K., 2007, in Shaw R. A., Hill F., Bell D. J., eds, *Astronomical Society of the Pacific Conference Series Vol. 376, Astronomical Data Analysis Software and Systems XVI*. p. 127

Offringa A. R., Smirnov O., 2017, *MNRAS*, 471, 301

Offringa A. R., McKinley B., Hurley-Walker et al., 2014, *MNRAS*, 444, 606

Offringa A. R., et al., 2015, *PASA*, 32, e008

Palmer J. E., et al., 2017, in *2017 IEEE Radar Conference (RadarConf)*. pp 1715–1720, [doi:10.1109/RADAR.2017.7944483](https://doi.org/10.1109/RADAR.2017.7944483)

Prabu S., Hancock P. J., Zhang X., Tingay S. J., 2020, *Publications of the Astronomical Society of Australia*, 37, e010

R. Sridharan A. F. P., 1998, *U.S. Space Surveillance Network capabilities*, [doi:10.1117/12.331225](https://doi.org/10.1117/12.331225), <https://doi.org/10.1117/12.331225>

The Astropy Collaboration et al., 2013, *Astronomy & Astrophysics*, 558, 9

Tingay S. J., et al., 2013a, *Publications of the Astronomical Society of Australia*, 30

Tingay S. J., et al., 2013b, *Astronomical Journal*, 146

Torbert S., 2016, *Applied computer science*. Springer

Tremblay S. E., et al., 2015, *PASA*, 32, e005

Wayth R. B., et al., 2018, *PASA*, 35

Zhang X., et al., 2018, *Monthly Notices of the Royal*

¹⁰<https://pypi.org/project/ephem/>

¹¹ds9.si.edu/site/Home.html

[Astronomical Society](#), 11, 1

van der Walt S., Colbert S. C., Varoquaux G., 2011,
[Computing in Science & Engineering](#), 13, 22